PNAS BRIEF REPORT | PHYSIOLOGY OPEN ACCESS

Identification of mEAK-7 as a human V-ATPase regulator via cryo-EM data mining

Longfei Wang[a,b,c,d,1], Di Wu[e,f], Carol V. Robinson[e,f], and Tian-Min Fu[g,h,1]

Edited by Nieng Yan, Princeton University, Princeton, NJ; received March 2, 2022; accepted July 9, 2022

Vacuolar-type adenosine triphosphatases (V-ATPases) not only function as rotary proton pumps in cellular organelles but also serve as signaling hubs. To identify the endogenous binding partners of V-ATPase, we collected a large dataset of human V-ATPases and did extensive classification and focused refinement of human V-ATPases. Unexpectedly, about 17% of particles in state 2 of human V-ATPases display additional density with an overall resolution of 3.3 Å. Structural analysis combined with artificial intelligence modeling enables us to identify this additional density as mEAK-7, a protein involved in mechanistic target of rapamycin (mTOR) signaling in mammals. Our structure shows that mEAK-7 interacts with subunits A, B, D, and E of V-ATPases in state 2. Thus, we propose that mEAK-7 may regulate V-ATPase function through binding to V-ATPases in state 2 as well as mediate mTOR signaling.

V-ATPase | lysosomal signaling | mEAK-7 | mTOR

Vacuolar-type adenosine triphosphatases (V-ATPases) are large protein complexes embedded in plasma membranes and membranes of cellular organelles and primarily function as proton pumps for maintaining intracellular pH homeostasis (1, 2). More recently, V-ATPases have been found to be crucial for mediating many signaling pathways, including Wnt, mTOR, and Notch signaling (3–6). Structural and biochemical studies have revealed that V-ATPases are composed of a cytosolic V_1 complex and a membrane-embedded V_o complex (7–10). Three rotational states of V-ATPases identified by structural studies indicate a rotary mechanism of proton transfer by V-ATPases, in which the V_1 complex can hydrolyze ATP to drive the rotation of the V_o complex for proton transfer (9, 11).

Many protein partners have been indicated to directly bind with V-ATPases for regulating V-ATPase activity as well as mediating V-ATPase–associated cell signaling (12–14). For example, NCOA7, RPS6KA3, WDR7, CCT8, CCT7, CCT6A, CCT2, CCT3, CCT4, and TCP1 have been shown to be associated with V-ATPases, through mass spectrometry analysis (12). To further confirm and identify V-ATPase binding partners, we collected a large cryoelectron microscopy (cryo-EM) dataset of human V-ATPases purified from HEK293 cells and did multiple rounds of classifications and focused refinements. Through our structural analysis, we found an additional density tightly associated with the V_1 complex in state 2 and assigned this density as mammalian Enhancer-of-Akt-1-7 (mEAK-7). Our structure reveals that mEAK-7 establishes extensive interactions with subunits V_1 and may regulate the function of V-ATPases.

Results

To identify low-abundance interacting partners of human V-ATPases, we first purified human V-ATPases from HEK293 cells in detergent lauryl maltose neopentyl glycol using a fragment of SidK, an effector protein from *Legionella pneumophila*, as reported before (9, 15). We collected more than 30,000 images at the cryo-EM center of National Cancer Institute. As published before, our first reconstruction allowed us to generate three maps corresponding to the three rotational states of V-ATPases (Fig. 1*A*). During further three-dimensional (3D) classification of these three rotational states, we recognized an additional density in one class that contains about 4.5% of particles in state 2, and we generated a mask of this density (Fig. 1*A*). After another round of 3D classification and focused refinement using the mask generated, we identified three classes that display an additional density tightly associated with the V_1 domain of V-ATPases (Fig. 1*A*). Of these three classes, one class that contains 5% of total particles (16.6% of particles in state 2) gives rise to a structure with an overall resolution of 3.3 Å, which allows us to unambiguously assign most residues (Fig. 1 *A*–*C* and *SI Appendix*, Table S1). However, due to the limited local resolution of the newly identified density in V-ATPases, we cannot build a de novo model of this region. To identify this V-ATPase binding partner, we first selected potential V-ATPase–interacting proteins

Author affiliations: [a]Department of Cardiology, Zhongnan Hospital of Wuhan University, School of Pharmaceutical Sciences, Wuhan University, Wuhan 430071, China; [b]Wuhan Research Center for Infectious Diseases and Cancer, Chinese Academy of Medical Sciences, Wuhan 430071, China; [c]Department of Cardiovascular Surgery, Zhongnan Hospital of Wuhan University, Wuhan 430071, China; [d]Key Laboratory of Combinatorial Biosynthesis and Drug Discovery, Ministry of Education and School of Pharmaceutical Sciences, Wuhan University, Wuhan 430071, China; [e]Department of Chemistry, University of Oxford, Oxford OX1 3QZ, United Kingdom; [f]Kavli Institute for Nanoscience Discovery, University of Oxford, Oxford OX1 3QZ, United Kingdom; [g]Department of Biological Chemistry and Pharmacology, The Ohio State University, Columbus, OH 43210; and [h]The Ohio State University Comprehensive Cancer Center, Columbus, OH 43210

Author contributions: L.W. and T.-M.F. designed research; L.W., D.W., and T.-M.F. performed research; L.W., C.V.R., and T.-M.F. analyzed data; and L.W. and T.-M.F. wrote the paper.

The authors declare no competing interest.

[1]To whom correspondence may be addressed. Email: Wanglf@whu.edu.cn or Fu.978@osu.edu.

This article contains supporting information online at http://www.pnas.org/lookup/suppl/doi:10.1073/pnas.2203742119/-/DCSupplemental.

Published August 22, 2022.

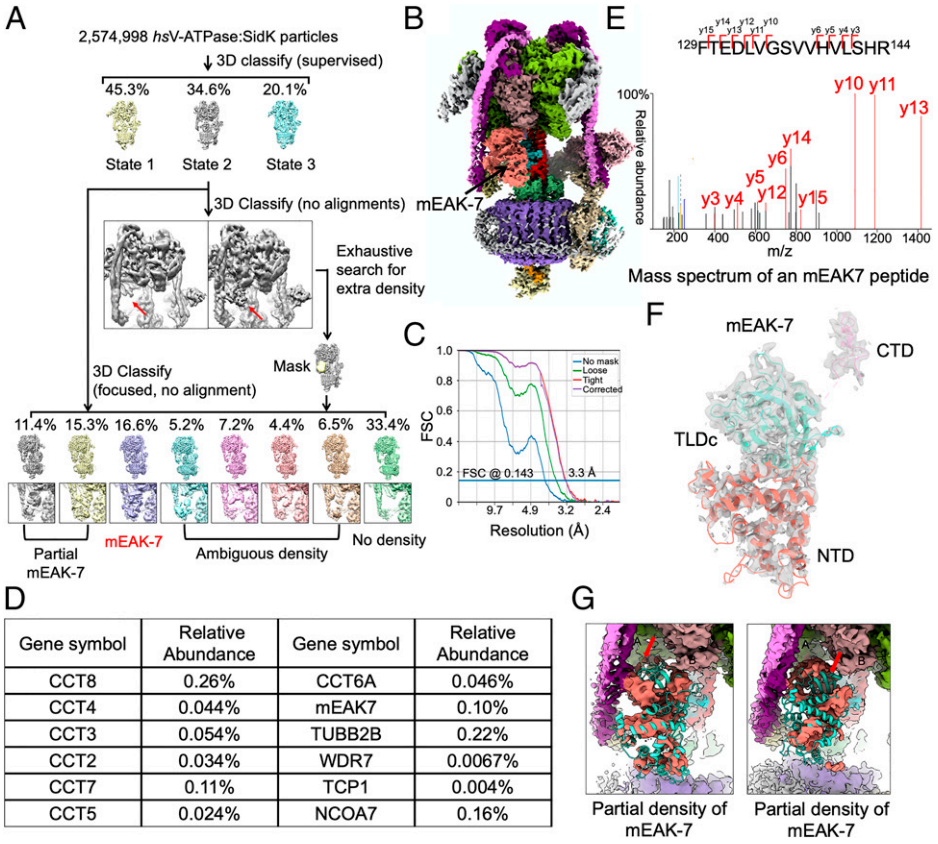

D

Gene symbol	Relative Abundance	Gene symbol	Relative Abundance
CCT8	0.26%	CCT6A	0.046%
CCT4	0.044%	mEAK7	0.10%
CCT3	0.054%	TUBB2B	0.22%
CCT2	0.034%	WDR7	0.0067%
CCT7	0.11%	TCP1	0.004%
CCT5	0.024%	NCOA7	0.16%

Fig. 1. Identification of mEAK-7 as a V-ATPase binding partner. (*A*) A diagram of V-ATPases cryo-EM data processing. The best class containing mEAK-7 is highlighted in red. The mEAK-7 binding site is pointed out using red arrows. (*B*) Cryo-EM density of human V-ATPase in complex with mEAK-7 with all the subunits color coded; mEAK-7 is highlighted in salmon. (*C*) Fourier shell correlation (FSC) curves of 3D reconstructed human V-ATPase map. (*D*) Representative V-ATPases binding partners identified by mass spectrometry and their relative abundance. (*E*) The mass spectrometry fingerprint of a representative mEAK-7 peptide. (*F*) Structural model of mEAK-7 fitted into a cryo-EM density map with domains color coded. (*G*) Cryo-EM density maps of the other two classes that contain partial density of mEAK-7.

that were identified in our purified V-ATPase sample by mass spectrometry, including mEAK-7, WDR7, CCT2, CCT5, CCT6A, CCT8, and NCOA7 (Fig. 1 *D* and *E*), and fitted their structural models predicted by AlphaFold into our density map (16). Among our candidate proteins, we found that mEAK-7 fitted best with the density (Fig. 1*F*). As a signaling protein anchored in lysosome membranes via an N-terminal myristoyl-glycine (17, 18), mEAK-7 is composed of three domains: the N-terminal domain of nine short **α**-helices domains (NTD), a TLDc (Tre2/Bub2/Cdc16 lysin motif domain catalytic) fold with 12 **β**-strands, and a C-terminal domain (CTD) containing short **α**-helices (Fig. 1*F*). Due to the resolution limitation of CTD, we cannot register residues in this motif. Moreover, the linker between TLDc and CTD was absent in our structure (Fig. 1*F*). In addition to the class with intact mEAK7 density, we also identified two classes with partial densities of mEAK-7 by 3D classification focusing on the mEAK7 region, suggesting the plasticity of mEAK-7 in V-ATPase engagement (Fig. 1*G*).

Earlier structural studies have captured three rotational states of V-ATPases, which are related to each other by 120° (9, 11). Unexpectedly, mEAK-7 was observed only in state 2 but not in other states (Fig. 1*A*), indicating that mEAK-7 may prefer binding to the V-ATPases in state 2 and thereby regulate the activity of V-ATPases. The mEAK-7 utilize the conserved TLDc domain and CTD to establish extensive interactions with V-ATPases, while the NTD of mEAK-7 has no contacts with any subunits of V-ATPases (Fig. 2*A*). Subunits A and B in the V_1 complex form three pairs of heterodimers with three conformations, denoted as AB_{open}, AB_{closed}, and AB_{semi} (Fig. 2*B*). The TLDc domain interacts with subunits E, A_{closed}, and B_{semi} with a buried surface area of 1,500 $Å^2$ (Fig. 2 *A* and *B*). The interfaces between TLDc and subunits E, A_{closed}, and B_{semi} are dominated by hydrophilic interactions (Fig. 2 *C*–*E*). As the three pairs of AB heterodimers display three different conformations, the TLDc domain binds to the B_{semi} subunits, thus placing the CTD of mEAK-7 in the cavity of the AB_{semi} heterodimer (Fig. 2*B*). While the CTD of mEAK-7 established limited interactions with A_{semi}, it formed extensive interactions with subunits B_{semi} and D (Fig. 2*F*). Given that subunit D is responsible for transmitting the torque through rotations induced by conformational changes of AB heterodimers, the extensive interactions between mEAK-7 CTD and subunit D may block the rotation of subunit D to impair the torque transmission. Compared with the apo V-ATPases in state 2, mEAK-7–bound V-ATPases display obvious conformational changes in the V_1 complex that include the positional shift of subunits E, G, and a few helices in B_{semi} and A_{semi} moving away from subunit D (Fig. 2 *G* and *H*).

Discussion

Here, we identified mEAK-7 as a V-ATPase–associated regulator that may regulate the function of the human V-ATPases. The mEAK-7 establishes extensive interactions with subunits in the V_1 complex and prefers to bind the human V-ATPases in state 2. During the preparation of this manuscript, Tan et al. (19) posted a discovery similar to ours, in bioRxiv. In addition, Tan et al. also observed an additional C subunit density in some classes, which was not observed in our maps. Perhaps V-ATPases have different compositions in different tissues and cells, and the different sources for V-ATPase purification between us and Tan et al. lead to the divergence of reconstructed V-ATPase maps. Moreover, although the structural analysis indicates that mEAK-7 may inhibit the proton transfer by locking the V-ATPase in state 2, biochemical and cellular assays showed that mEAK-7 cannot effectively inhibit the activity of V-ATPases both in vitro and in cells (19). Perhaps the ATP hydrolysis by the V_1 complex may be able to disrupt the

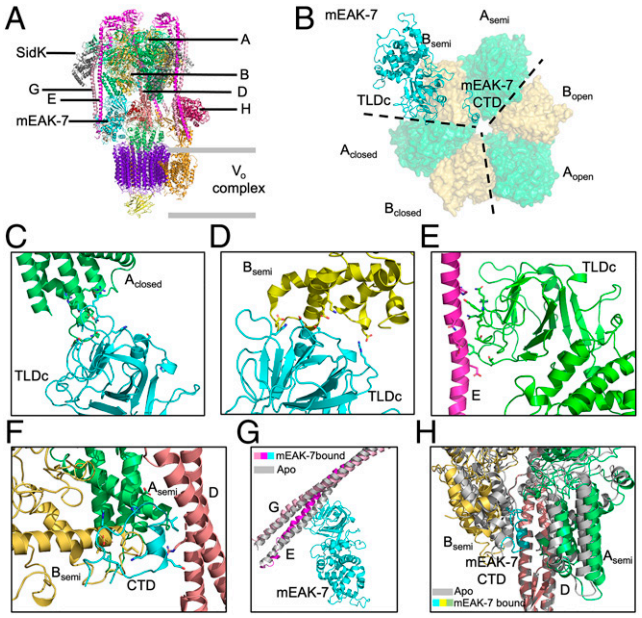

Fig. 2. Structures and interactions of mEAK-7 and the V-ATPase. (*A*) Ribbon diagram of V-ATPase structure in complex with mEAK-7; mEAK-7 is highlighted in green. (*B*) Surface representation of AB heterodimers in complex with ribbon diagram of mEAK-7 (green). The three pairs of AB heterodimers are denoted as AB_{open}, AB_{closed}, and AB_{semi}. (*C*) Detailed interactions of subunit A_{closed} with TLDc domain of mEAK-7. (*D*) Detailed interactions of subunit B_{semi} with TLDc domain of mEAK-7. (*E*) Detailed interactions of subunit E with TLDc domain of mEAK-7. (*F*) Interactions of mEAK-7 CTD with subunits A_{semi}, B_{semi}, and D. (*G*) Structural comparison of subunits EG in apo state (apo) and mEAK-7–bound state (color coded). (*H*) Structural comparison of subunits A_{semi}, B_{semi} and D in apo state (apo) and mEAK-7–bound state (color coded).

interactions between mEAK-7 and V-ATPases during proton transfer (20). Consistently, we observed partial dissociation of mEAK-7 from subunits A or B (Fig. 1*G*), which could explain why mEAK-7 cannot withstand the conformational changes of the V_1 complex during ATP hydrolysis. Thus, the binding of mEAK-7 to V-ATPases may have other physiological roles in cells. As earlier studies have shown that mEAK-7 serves as an activator of mTORC1 signaling by facilitating the recruitment of mTORC1 to lysosomes (18), it is possible that mEAK-7 may serve as an adaptor protein to link mTORC1 with V-ATPases. But the exact mechanism of how mEAK-7 links mTORC1 and V-ATPase remains to be explored. Our current study opens the door for future study on the roles of mEAK-7 in mTORC1 signaling and V-ATPase regulation.

Materials and Methods

Purification and Cryo-EM Grid Preparation of Human V-ATPases. The purification and cryo-EM grid preparation of human V-ATPases followed the protocol published before (15).

Data Collection and Processing. Data were collected using a 300-kV Titan Krios microscope (FEI) equipped with a K3 direct electron detector (Gatan); 30,446 micrographs were collected in counting mode, with 40 total frames per movie, 1.5-s exposure time, 50.0 electrons per $Å^2$ accumulated dose, and 1.08-Å pixel size. Movies were motion corrected using MotionCor2 (20), the output micrographs were imported into cryoSPARC (21), and CTFFIND4 was used to perform contrast transfer function estimation (22). Particles were picked using Topaz with a general model (23). After initial 2D and 3D classifications, particles from rotational state 2 were further classified without alignments using the "3D Classification" program in cryoSPARC (21). Strong densities were identified between A, B, and E subunits, and another round of "3D Classification" was performed on this region using a mask; 16.6% of the particles from state 2 were selected for nonuniform refinement. This region with extra density was further improved using local refinement with a mask that also included the neighboring A, B, D, E, F, and G subunits. The local refinement map was sharpened using DeepEMhancer to assist model building (24).

Data, Materials, and Software Availability. Accession numbers for mEAK-7–bound V-ATPases are (coordinates of atomic models) Protein Data Bank (PDB), http://www.rcsb.org/, with a PDB code of 7U4T (25), and (density map) Electron Microscopy Data Bank, http://www.emdataresource.org, with a code of EMD-26334 (26). All the raw images of V-ATPases were deposited to the Electron Microscopy Public Image Archive, https://www.ebi.ac.uk/empiar/, with a code of EMPIAR-11132 (27). All other study data are included in the article and/or *SI Appendix*.

ACKNOWLEDGMENTS. Cryo-EM data were collected with the assistance of Drs. Adam D. Wier, Thomas J. Edwards, and Ulric Baxa at the National Cancer Institute Cryo-Electron Microscopy Center supported by a grant from the NIH National Institute of General Medical Sciences (Grant GM103310). T.-M.F. was supported by the Ohio State University startup fund and the NIH National Institute of General Medical Sciences (Grant 1R35GM147465).

1. M. Forgac, Vacuolar ATPases: Rotary proton pumps in physiology and pathophysiology. *Nat. Rev. Mol. Cell Biol.* **8**, 917–929 (2007).
2. V. Marshansky, J. L. Rubinstein, G. Grüber, Eukaryotic V-ATPase: Novel structural findings and functional insights. *Biochim. Biophys. Acta* **1837**, 857–879 (2014).
3. G. H. Sun-Wada, Y. Wada, Role of vacuolar-type proton ATPase in signal transduction. *Biochim. Biophys. Acta* **1847**, 1166–1172 (2015).
4. C. M. Cruciat *et al.*, Requirement of prorenin receptor and vacuolar H+-ATPase-mediated acidification for Wnt signaling. *Science* **327**, 459–463 (2010).
5. R. Zoncu *et al.*, mTORC1 senses lysosomal amino acids through an inside-out mechanism that requires the vacuolar H(+)-ATPase. *Science* **334**, 678–683 (2011).
6. T. Vaccari, S. Duchi, K. Cortese, C. Tacchetti, D. Bilder, The vacuolar ATPase is required for physiological as well as pathological activation of the Notch receptor. *Development* **137**, 1825–1832 (2010).
7. J. Zhao, J. L. Rubinstein, The study of vacuolar-type ATPases by single particle electron microscopy. *Biochem. Cell Biol.* **92**, 460–466 (2014).
8. Y. M. Abbas, D. Wu, S. A. Bueler, C. V. Robinson, J. L. Rubinstein, Structure of V-ATPase from the mammalian brain. *Science* **367**, 1240–1246 (2020).
9. L. Wang, D. Wu, C. V. Robinson, H. Wu, T. M. Fu, Structures of a complete human V-ATPase reveal mechanisms of its assembly. *Mol. Cell* **80**, 501–511.e3 (2020).
10. R. Wang *et al.*, Cryo-EM structures of intact V-ATPase from bovine brain. *Nat. Commun.* **11**, 3921 (2020).
11. J. Zhao, S. Benlekbir, J. L. Rubinstein, Electron cryomicroscopy observation of rotational states in a eukaryotic V-ATPase. *Nature* **521**, 241–245 (2015).
12. M. Merkulova *et al.*, Mapping the H(+) (V)-ATPase interactome: Identification of proteins involved in trafficking, folding, assembly and phosphorylation. *Sci. Rep.* **5**, 14827 (2015).
13. R. A. Saxton, D. M. Sabatini, mTOR signaling in growth, metabolism, and disease. *Cell* **168**, 960–976 (2017).
14. Y. Xu *et al.*, A bacterial effector reveals the V-ATPase-ATG16L1 axis that initiates xenophagy. *Cell* **178**, 552–566.e20 (2019).
15. L. Wang, Z. Chen, H. Wu, T. M. Fu, Purification and cryoelectron microscopy structure determination of human V-ATPase. *STAR Protoc* **2**, 100350 (2021).
16. J. Jumper *et al.*, Highly accurate protein structure prediction with AlphaFold. *Nature* **596**, 583–589 (2021).
17. K. Moriya *et al.*, Protein N-myristoylation plays a critical role in the endoplasmic reticulum morphological change induced by overexpression of protein Lunapark, an integral membrane protein of the endoplasmic reticulum. *PLoS One* **8**, e78235 (2013).
18. J. T. Nguyen *et al.*, Mammalian EAK-7 activates alternative mTOR signaling to regulate cell proliferation and migration. *Sci. Adv.* **4**, eaao5838 (2018).
19. Y. Z. Tan *et al.*, CryoEM of endogenous mammalian V-ATPase interacting with the TLDc protein mEAK-7. *bioRxiv* [Preprint] (2022). https://doi.org/10.1101/2021.11.03.466369 (Accessed 9 August 2022).
20. S. Q. Zheng *et al.*, MotionCor2: Anisotropic correction of beam-induced motion for improved cryo-electron microscopy. *Nat. Methods* **14**, 331–332 (2017).
21. A. Punjani, J. L. Rubinstein, D. J. Fleet, M. A. Brubaker, cryoSPARC: Algorithms for rapid unsupervised cryo-EM structure determination. *Nat. Methods* **14**, 290–296 (2017).
22. A. Rohou, N. Grigorieff, CTFFIND4: Fast and accurate defocus estimation from electron micrographs. *J. Struct. Biol.* **192**, 216–221 (2015).
23. T. Bepler *et al.*, Positive-unlabeled convolutional neural networks for particle picking in cryo-electron micrographs. *Res. Comput. Mol. Biol.* **10812**, 245–247 (2018).
24. R. Sanchez-Garcia *et al.*, DeepEMhancer: A deep learning solution for cryo-EM volume post-processing. *Commun. Biol.* **4**, 874 (2021).
25. L. Wang, T. M. Fu, Human V-ATPase in state 2 with SidK and mEAK-7. Protein Data Bank. http://www.rcsb.org/pdb/explore/explore.do?structureId=7U4T. Deposited 1 March 2022.
26. L. Wang, T. M. Fu, Human V-ATPase in state 2 with SidK and mEAK-7. Electron Microscopy Data Bank. https://www.ebi.ac.uk/emdb/EMD-26334. Deposited 1 March 2022.
27. L. Wang, H. Wu, T. M. Fu, Cryo-EM structures of human V-ATPase. Electron Microscopy Public Image Archive. https://www.ebi.ac.uk/empiar/EMPIAR-11132/. Deposited 4 August 2022.